Particle
& Particle Systems Characterization
www.particle-journal.com

Laser-Scanning Microscopy for Electrophoretic Mobility Characterization of Single Nanoparticles

Lucas Oorlynck, Yera Ye. Ussembayev, Ingrid Amer Cid, Juan Fraire, Charlotte Hinnekens, Kevin Braeckmans, and Filip Strubbe**

To enable detailed studies of interactions between nanoparticles and their environment and the correlations between various nanoparticle properties, one must go beyond ensemble averages and toward single-particle measurements. However, current methodologies for the single-nanoparticle analysis of charge and size either lack the flexibility to study dynamic processes on the single-particle level or are highly specific and require complex microfluidic devices. In addition, accurate measurements of the electrophoretic mobility (or zeta-potential) based on the optical detection of single nanoparticles remain challenging due to the low photon budget, the required sampling frequency, and the fact that electroosmosis in typical microfluidic devices must be analyzed carefully. In this study, a method is investigated to accurately characterize the electrophoretic mobility of individual nanoparticles and estimate their size by simultaneously analyzing the electrokinetic- and Brownian motion in a simple microfluidic channel. Fast laser scanning excitation and sensitive detection of fluorescent photons enable single-nanoparticle velocimetry experiments in an oscillating electric field at high frame rates.

1. Introduction

Nanoparticles are encountered in a wide range of biomedical and nanotechnological applications. They come in different forms, from man-made materials such as nanocrystals to vesicles in living organisms. In addition they have a large variety of physical and chemical properties such as size, shape, charge, luminescence, and surface composition, that often play a crucial role in their behavior and functionality. Together with the increasing use and demand of nanoparticle-based applications such as: targeted drug delivery,[1,2] gene delivery,[3,4] RNA therapeutics,[5,6] and biosensing,[7–10] the need for better understanding of biomolecular interactions[11,12] and growing concerns toward endocytosis of potentially toxic nanomaterials,[13,14] there is an accompanying need for more sophisticated nanoparticle characterization tools.

For basic characterization of the size and charge of nanoparticles, a variety of measurement techniques are available. Size measurements on the ensemble level can be carried out using dynamic light scattering (DLS), fluorescence correlation spectroscopy (FCS), or X-ray diffraction (XRD). On a particle-to-particle basis one can use resistive pore sensing (RPS), nanoparticle tracking analysis (NTA), atomic force microscopy (AFM), or electron microscopy (EM). For charge characterization, frequently used techniques are electrophoretic light scattering (ELS) (a combination of laser Doppler electrophoresis and phase analysis light scattering (PALS)) and Western blot. In recent years, also several more advanced techniques have been developed for the sensitive characterization of nanoparticles on a particle-to-particle basis. For example, tunable resistive pore sensing (tRPS) is used to measure the size and zeta-potential of individual nanoparticles.[15] And also by passively-[11,16,17] or actively[12,18–20] trapping nanoparticles with electric fields, or by tethering them to a surface,[21] an accurate characterization of individual nanoparticles is achieved. However, current methods are often tailored to specific particles, require complex microfluidics, and are limited in their multi-parameter capabilities (a comprehensive table is provided in Supporting Information).

In this work, we focus on accurate measurements of the electrophoretic mobility of individual nanoparticles in their native liquid environment. To achieve this, we combine standard particle velocimetry measurements in the presence of an electric field with advanced imaging developed originally for single-molecule analysis. We use acousto-optic deflectors to scan a tightly focused laser beam in a pixel-matrix pattern and synchronously record the photon count using a single-photon counting module and an FPGA (field-programmable gate array) to visualize fluorescent polystyrene (PS) nanoparticles, similar

L. Oorlynck, Y. Ye. Ussembayev, I. A. Cid, F. Strubbe
Department of Electronics and Information Systems
Ghent University
Tech Lane Ghent Science Park - Campus A 126, 9052 Ghent, Belgium
E-mail: lucas.oorlynck@ugent.be; filip.strubbe@ugent.be
J. Fraire, C. Hinnekens, K. Braeckmans
Laboratory for General Biochemistry and Physical Pharmacy
Faculty of Pharmaceutical Sciences
Ghent University
9000 Ghent, Belgium
The ORCID identification number(s) for the author(s) of this article can be found under https://doi.org/10.1002/ppsc.202200152.

DOI: 10.1002/ppsc.202200152

to the Anti-Brownian Electrokinetic (ABEL)-trap illumination scheme.[12] In this way, we obtain sensitive images at frame rates of several thousand frames per second. This technique is applied to the electrophoresis of fluorescent nanoparticles having sizes between 100 and 500 nm in water. Crucially, in order to obtain accurate electrophoretic mobility, the influence of electroosmosis in the microchannel is taken into account. A thorough analysis is carried out of the electroosmotic flow as a function of position in the channel and of the frequency and amplitude of the applied field, and this turns out to agree well with a theoretical model. Also, the size is estimated from the Brownian motion analysis.

The presented technique can be further developed such that a broader range of parameters can be measured simultaneously on a single-particle level, and if desired it may also be combined with active trapping. In this way, it forms a versatile multi-parameter analysis tool that can be used for relatively high throughput characterization of polydisperse samples as well as for detailed long-term studies of single particles.

2. Results and Discussion

2.1. Laser Scanning Microscopy of Single Nanoparticles in an Electric Field

To track single nanoparticles (NPs) free in solution we developed an FPGA-controlled laser-scanning microscope. The FPGA synchronously applies a voltage difference (AC) across a microchannel, reads out the photon count from a single-photon counting module (SPCM), and drives the acousto-optic deflectors to scan the laser beam. **Figure 1** illustrates the experimental setup and the different steps to transform the acquired input and output signals of the FPGA into a particle trace. As shown in Figure 1a, a 532 nm diode laser is deflected in two orthogonal planes which, through some relay optics, results in a lateral displacement of the laser focus in the focal plane (the (x, y)-plane) of the microscope objective. When a NP is present in the confocal volume, it emits fluorescent light with a longer wavelength which is captured by the same microscope objective used for laser-scanning (i.e., epifluorescence). Using a dichroic mirror the emitted fluorescent photons are separated from the excitation light and after the dichroic mirror, an additional bandpass filter is added to further enhance the dichroic filtering. The resulting filtered fluorescent light is then transmitted to the SPCM and CMOS camera. By synchronously counting photons and driving the AODs at a high frequency, information on the location and intensity of the fluorescent light is obtained. The laser-scanning and photon-by-photon capturing scheme controlled by an FPGA is based on the ABEL-trap scheme developed at the Moerner Lab.[19,22]

Figure 1b illustrates the grid scanning pattern and the resulting reconstructed nanoparticle image. In Figure 1b(i) the laser scanning along an "S"-shaped path is shown schematically for a regular 5×5-grid (in reality 16×16). Each pixel position (m, n) with $m = \{1, ..., M\}$ and $n = \{1, ..., N\}$ is associated with a pixel number $i = \{1, ..., M \times N\}$ and a fluorescent photon count $I_i = I(m, n)$. In this schematic example, a NP emitting fluorescent light is present roughly in the center of the scanned grid. Figure 1b(ii) shows an actual CMOS image (10 ms integration time) of a 16×16 pixel grid with a pixel spacing of ≈410 nm and a pixel dwell time (time between subsequent laser positions) of 1.15 µs resulting in a total image of 6.15 µm × 6.15 µm with a total scan time close to 300 µs. Since the integration time of the CMOS camera is 33 times longer than the time for scanning of the pixel grid, the scanned area shows up as an evenly illuminated square (the dark edge shows the background outside of the illuminated area). In the center of the CMOS image, the fluorescent light emitted by a stuck 100 nm particle is visible. To limit the noise contribution from fluorescent photons outside

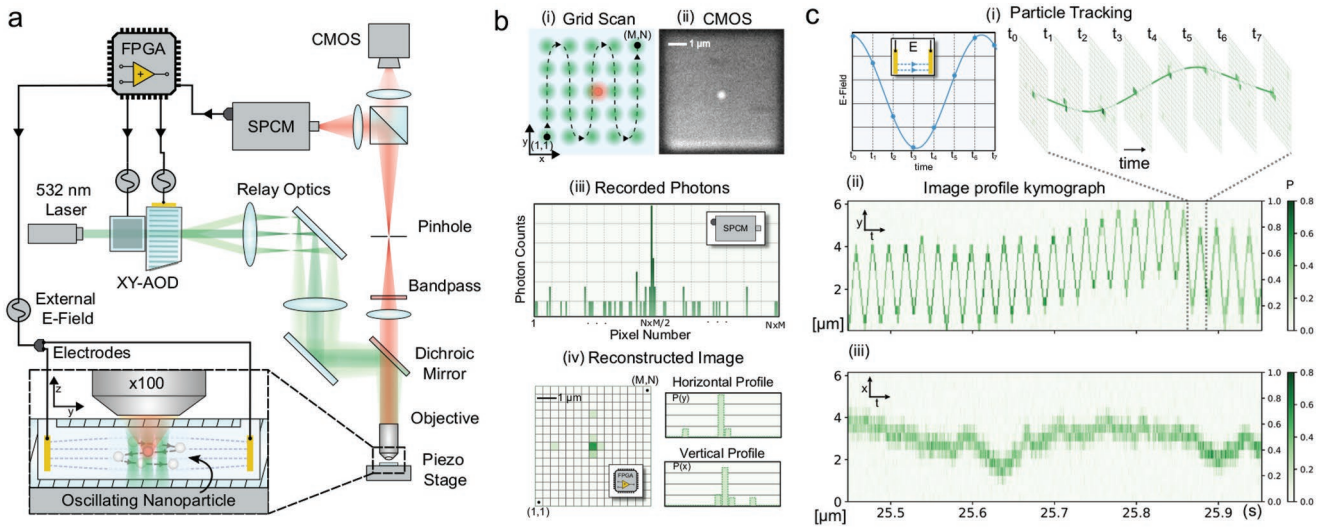

Figure 1. a) Schematic overview of the experimental setup, showing the illumination optics, FPGA synchronization and the microfluidic device. b) Schematic representation of a grid scan (i) and complementary CMOS image (ii) of a particle in the center of the image. Actual photon count data per pixel for a particle in the FOV (iii) and reconstructed frame (iv). c) Illustration of the applied electric field and the resulting particle images over time (i). Kymographs (actual data) of a single 100 nm particle oscillating at 50 Hz in the y-direction (ii) and moving freely in the x-direction (iii), recorded at 3300 fps.

of the scanning region a pinhole with a diameter of 1 mm is placed in the first conjugate plane of the microscope objective. This pinhole corresponds to a 10 µm field-of-view (FOV) in the focal plane of the sample. Figure 1b(iii,iv) respectively show the photon count per pixel and the reconstructed image based on actual data of a single 100 nm particle in the center of the scanning area. The signal-to-noise ratio of a 100 nm particle is close to 5 for a particle near the focal plane. If the particle diffuses in the *z*-direction away from the focal plane, its signal-to-noise ratio rapidly diminishes to 1, this is a consequence of the large contribution to the background signal by other fluorescent particles within the FOV but beyond the depth of focus, that is, if a particle is more than 1.4 µm away from the focal plane (however, other noise sources such as stray light, imperfect confocal imaging, autofluorescence, and improper dichroic filtering also reduce the SNR, especially so for smaller NPs with low photon budget). By diluting the NP suspension the background signal can be reduced further however, this prolongs the time between particles entering the FOV and increases the experiment run time. This is undesired since it leads to an increased temperature in the microfluidic channel, due to continuously applying an AC field. Consequently, the increased temperature influences the viscosity of the liquid medium,[23,24] which reduces the accuracy of the mobility and diffusivity values if the temperature is not tracked during the measurement. Therefore an intermediate particle concentration (see Experimental Section) and measurement duration were chosen. Figure 1b(iv) also shows the intensity profiles along the *x*- and *y*-direction $P_x = P(m) = \sum_{n=1}^{N} I(m,n)$ and $P_y = P(n) = \sum_{m=1}^{M} I(m,n)$, which are used for tracking the particle motion.

By repetitively scanning the pixel matrix and applying a periodic (AC) electric field (generated by applying a voltage difference between the electrodes) in the *y*-direction, a series of images is obtained in which the NP trajectory can be identified by way of centroid tracking (details see Experimental Section) as shown in Figure 1c(i). Figure 1c(ii) shows the kymographs (i.e., time series of the integrated profiles P_x and P_y) of the *x*-intensity profile of a 100 nm particle oscillating at 50 Hz at a frame rate of 3300 frame per second, and Figure 1c(iii) shows a similar plot for the *y*-direction. As can be seen from the kymographs, and as expected, the NP demonstrates a combination of an oscillation and Brownian motion in the *y*-direction, and only Brownian motion in the *x*-direction. The movement along the *y*-direction is dominated by the combined electrophoretic and electroosmotic motion. The particle remains within the FOV for over 0.5 s and is easily distinguishable from the background. The Brownian motion shows no preferred direction, confirming that no pressure difference exists between both ends of the channel as was intended by the sample design (see Experimental Section and Supporting Information).

2.2. Validation of the Model for Electrophoresis and Electroosmosis

The motion of a particle in the considered open microfluidic channel, with equal pressure at inlet and outlet and with an electric potential difference between the two terminals, has three contributions: Brownian, electrophoretic, and electroosmotic motion. However, the contribution of Brownian motion is rather small compared to the electrokinetic motion (in the case of our experimental parameters). Hence, the particle velocity $v_p(t)$ in an electric field $E(t) = E\sin(\omega t)$, with E the electric field strength and ω the angular frequency, can be described in good approximation by considering only the contributions from electrophoresis and electroosmosis[24]

$$v_p(t) = v_{ep}\sin(\omega t) + \alpha(f,z)\,v_{eo}\sin\left(\omega t + \beta(f,z)\right) \quad (1)$$

The electrophoretic velocity $v_{ep}(t)$ has a uniform response across the *z*-direction (same reference system as Figure 1a) in the microfluidic channel, proportional to the electric field[25] In contrast, the electroosmotic velocity depends on the *z*-coordinate and on the electric field frequency *f*. As ions in the electric double layers near the interfaces of the microchannel migrate under the influence of the electric field, they will induce a net flow in the boundary fluid layer.[26] Due to viscous drag, the influence of this net flow gets transferred to the bulk where it induces a periodic flow with a phase delay β and a dimensionless amplitude factor α, which both depend on the position *z* and frequency *f*. The full form of the dimensionless amplitude factor and phase delay are derived in Chun Yang et al.[26] (also see Supporting Information).

Since the parameters *z* and *f* are known in our experiments, both $\alpha(f, z)$ and $\beta(f, z)$ can be calculated, leaving only v_{ep} and v_{eo} as unknowns. By segmenting the velocity trace of the NP per period of the electric field and fitting the velocity amplitude to each segment we obtain a distribution of v_{ep} and v_{eo} for every particle (see Supporting Information).

Figure 2a shows the segmented velocity periods of a single 100 nm polystyrene particle oscillating at 75 Hz and located at the center plane of the microchannel (i.e., $z = 0$ µm, the boundaries of the microchannels are then respectively $z = -50$ µm and $z = 50$ µm for a 100 µm microchannel height). At this location and frequency, the assumed experimental parameters (see Experimental Section) give an amplitude factor $\alpha = 0.88$ and phase offset $\beta = -35.0°$ for the electroosmotic velocity contribution. As mentioned before, using these α and β values, Equation (1) is fitted to all individual periods using v_{ep} and v_{eo} as the fitting variables. The average velocity (dotted curve) of the measured particle, averaged over $n = 53$ periods, has an amplitude $|\overline{v}_p| \pm \sigma_{|\overline{v}_p|} = 0.50\,\mathrm{mm\,s^{-1}} \pm 0.06\,\mathrm{mm\,s^{-1}}$ and a phase $\phi(\overline{v}_p) \pm \sigma_{\phi(\overline{v}_p)} = -89.6° \pm 5.7°$. As a result the average fitted velocities are $\overline{v}_{ep} \pm \sigma_{\overline{v}_{ep}} = -0.70\,\mathrm{mm\,s^{-1}} \pm 0.10\,\mathrm{mm\,s^{-1}}$ and $\overline{v}_{eo} \pm \sigma_{\overline{v}_{eo}} = 0.97\,\mathrm{mm\,s^{-1}} \pm 0.11\,\mathrm{mm\,s^{-1}}$. Through division of the fitted velocities by the applied voltage V across the microfluidic channel we obtain the normalized fitted velocities $\hat{v}_{ep} = v_{ep}/V$ and $\hat{v}_{eo} = v_{eo}/V$ in units of mm V^{-1} s^{-1}. Figure 2b shows the distribution of the normalized fitted velocities $\hat{v}_{ep}$ and $\hat{v}_{eo}$ of the single particle from Figure 2a (crosses). This shows that the method produces reproducible values of the normalized electrophoretic and electroosmotic velocities per NP. Similar results for 81 other NPs of the same batch, measured in the same suspension and microfluidic channel but at different heights, frequencies and voltages, are also shown (circles). The average normalized fitted velocities are $\hat{\overline{v}}_{ep} \pm \sigma_{\hat{\overline{v}}_{ep}} = -0.07\,\mathrm{mm\,V^{-1}\,s^{-1}} \pm 0.03\,\mathrm{mm\,V^{-1}\,s^{-1}}$ and $\hat{\overline{v}}_{eo} \pm \sigma_{\hat{\overline{v}}_{eo}} = 0.11\,\mathrm{mm\,V^{-1}\,s^{-1}} \pm 0.03\,\mathrm{mm\,V^{-1}\,s^{-1}}$ (diamond).

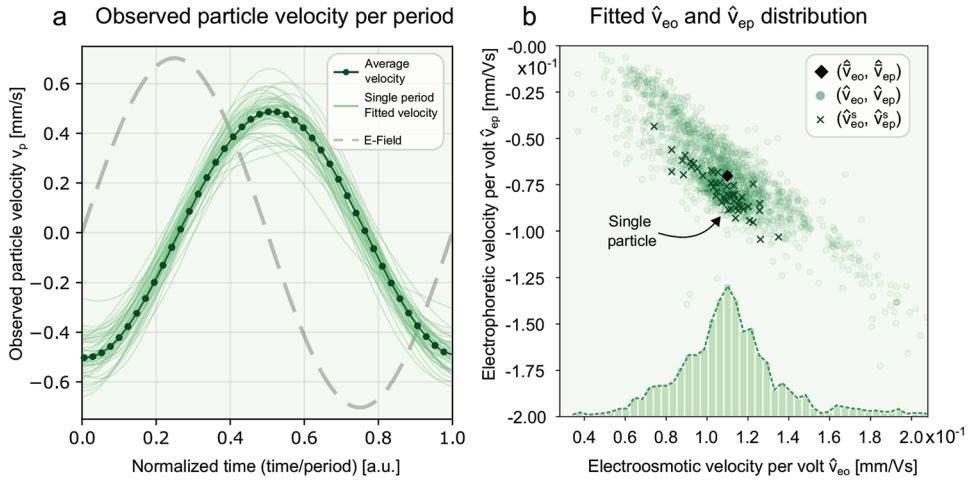

Figure 2. a) Overlapping filtered velocity periods (53 periods) of a single 100 nm particle oscillating at 75 Hz measured at the microchannel center plane ($z = 0$ µm). The average velocity $\overline{v}_p$ (dotted line) has an amplitude $|\overline{v}_p| = 0.5\text{mms}^{-1}$ and phase $\phi(\overline{v}_p) = -89.6°$. b) Scatter plot of more than 2000 normalized electrophoretic- and electroosmotic velocities based on 81 particles of 100 nm in the same suspension and microchannel. The diamond represents the population average and the crosses represent the data point from Figure 2a.

Interestingly, a strong anti-correlation ($\sigma^2_{ep,eo}/\sigma_{ep}\sigma_{eo} = -0.87$) is observed between $\hat{v}_{ep}$ and $\hat{v}_{eo}$. This can be understood from Equation (1) and artifacts from the spatial resolution of the imaging. As the pixel pitch of the laser-scanning grid is 410 nm, the amplitude resolution of the particle oscillation is limited. This causes both over- and under estimations of the particle oscillation amplitude. If two velocity periods v_{p1} and v_{p2} have different amplitudes $|v_{p1}| \neq |v_{p2}|$ but similar phase $\phi(v_{p1}) = \phi(v_{p2})$ and the same α and β values, then the ratio between v_{eo} and v_{ep} remains constant or $\frac{v_{eo1}}{v_{ep1}} = \frac{v_{eo2}}{v_{ep2}}$ (see Supporting Information) causing a spread of the single period velocity estimations and therefore an anti-correlation.

Figure 3 compares the measured data (same data as in Figure 2b) with the particle velocity model based on the average normalized fitted velocities $\overline{\hat{v}}_{ep}$ and $\overline{\hat{v}}_{eo}$. Figure 3a shows the dependency of the fitted (non-normalized) velocities to the applied voltage V. As expected, the absolute values of the electrophoretic and electroosmotic velocities increase proportionally to the voltage. In Figure 3b the frequency dependence of the particle velocity v_p at the center plane (i.e., $z = 0$ µm) is displayed. As the frequency increases from 50 to 100 Hz, the electroosmotic contribution reduces in amplitude (due to a decrease of α) and the phase offset will increase (due to a decrease of β). Together with the electrophoretic velocity (which has a −180° phase), this leads to an increasing combined amplitude and more out-of-phase response for increasing frequency. Finally, Figure 3c shows the influence of the z-position on the particle velocity v_p at a 75 Hz frequency. Similar to the frequency dependence, both the amplitude and phase vary with the z-position. When the particle is located more closely to the channel walls, the electroosmotic flow will reach the particle more quickly (hence $\beta \to 0$) and with less reduction of its amplitude (hence $\alpha \to 1$) resulting in a particle velocity $v_p \approx v_{eo} + v_{ep}$.

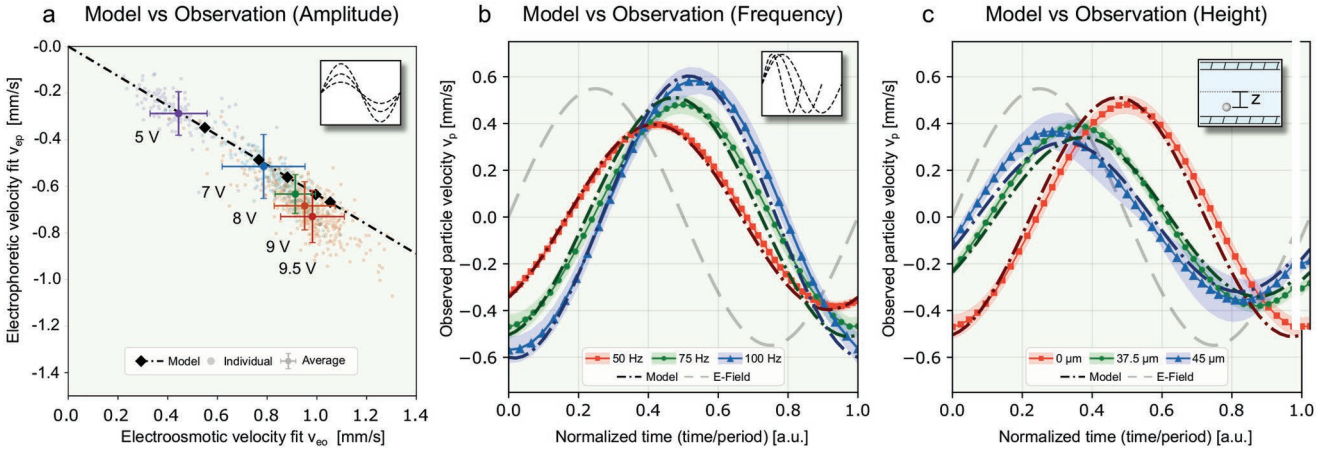

Figure 3. Measurement showing the agreement between the theoretical model (Equation (1)) and measurements of 100 nm particles using different experimental parameters. a) Scatter plot of fitted electrophoretic- and electroosmotic velocities for different applied voltages. b) Frequency dependency of the particle velocity. c) Dependency on the z-position of the particle velocity.

Overall, Figure 3 demonstrates that the observed dependencies of the electrophoretic and electroosmotic velocities with voltage amplitude, frequency, and z-position are consistent with the model.

2.3. Electrophoretic Mobility

In the previous section we observed that the particle velocity $v_p(t)$ follows the proposed model in Equation (1) well. However, rather than normalized velocities, it is desired to obtain the electrophoretic mobility μ_{ep} defined as the electrophoretic velocity divided by the electric field strength or $\mu_{ep} = v_{ep}/E$, expressed in mm^2 V^{-1} s^{-1}. Similarly one can define the electroosmotic mobility μ_{eo} as $\mu_{eo} = v_{eo}/E$. Using these definitions for μ_{ep} and μ_{eo} we can rewrite Equation (1) as follows

$$v_p(t) = E\left[\mu_{ep}\sin(\omega t) - \alpha(f,z)\mu_{eo}\sin\left(\omega t + \beta(f,z)\right)\right] \quad (2)$$

Therefore, by knowing the electric field strength E at the particle location and the particle velocity $v_p(t)$ (obtained in the previous subsection) we can calculate the electrophoretic mobility μ_{ep}. The electric field strength E was estimated through an AC/DC Comsol simulation of the used microchannel (see Experimental Section and Supporting Information).

Next, to produce the final electrophoretic mobilities of all measured nanoparticles, we choose to use only the average value of the previously obtained normalized electroosmotic velocity $\hat{\overline{v}}_{eo}$, and then fit Equation (2) to find the electrophoretic mobility for each particle. This is a reasonable simplification as long as the same device, liquid, and pH are used since we can assume that the glass substrates of the microchannel will develop the same charge double layer in a homogeneous way across the surface, based on the work of Page et al.[27] and Dorwling-Carter et al.[28]

Figure 4 shows the obtained electrophoretic mobility distributions of 100 nm (Figure 4a) and 500 nm (Figure 4b) PS particles. These mobility distributions are also compared to electrophoretic light scattering measurements (ELS Malvern ZetaSizer) of the same suspensions. Figure 4a shows the same 100 nm particle measurements from Figure 2b. Comparing the measurements of a set of 81 particles ($\overline{\mu}_{ep} \pm \sigma_{\overline{\mu}_{ep}} = (-3.4 \pm 0.6)\times10^{-8}$ m^2 V^{-1} s^{-1}, green histogram) with the ELS measurements ($\overline{\mu}_{ep} \pm \sigma_{\overline{\mu}_{ep}} = (-3.5 \pm 0.9)\times10^{-8}$ m^2 V^{-1} s^{-1}, red histogram), a comparable population average is found. Notice that the ELS measurement shows a larger spread which could be attributed to the ensemble[29] measurement strategy and the large number of particles measured at once, whereas the single-particle-based distribution consists of only 81 particles. In comparison to these population statistics, it can be observed that a single particle measurement shows a significantly narrower spread. In the case of the selected particle an average mobility of $\overline{\mu}_{ep} = -3.9\times10^{-8}$ m^2 V^{-1} s^{-1} and a standard deviation $\sigma_{\overline{\mu}_{ep}} = 0.3\times10^{-8}$ m^2 V^{-1} s^{-1} (about three times smaller) was measured out during a 0.75 s observation (55 velocity periods).

The 500 nm particles shown in Figure 4b were measured in a different microfluidic sample. Both the ELS and single particle measurements show narrower distributions.

Overall the mobility measurement distributions match well with the ELS measurements, though the 500 nm particles do show a more significant overestimation (more negative value) of the average electrophoretic mobility $\overline{\mu}_{ep}$. Since an identical suspension was used for the ELS and our particle measurements one would expect equal averages, as is the case for the 100 nm particles. However, this deviation is easily explained by taking into account the float range (±0.25 mm) of the electrodes at the microfluidic inlet and outlet. For a single experiment using the same microfluidic sample, the electrodes are fixed over the duration of said experiment. However, since the electrodes are submerged in the reservoirs manually the electrode spacing can change from microfluidic sample to microfluidic sample causing a maximum deviation of 10% on the field strength between a real experiment and the field

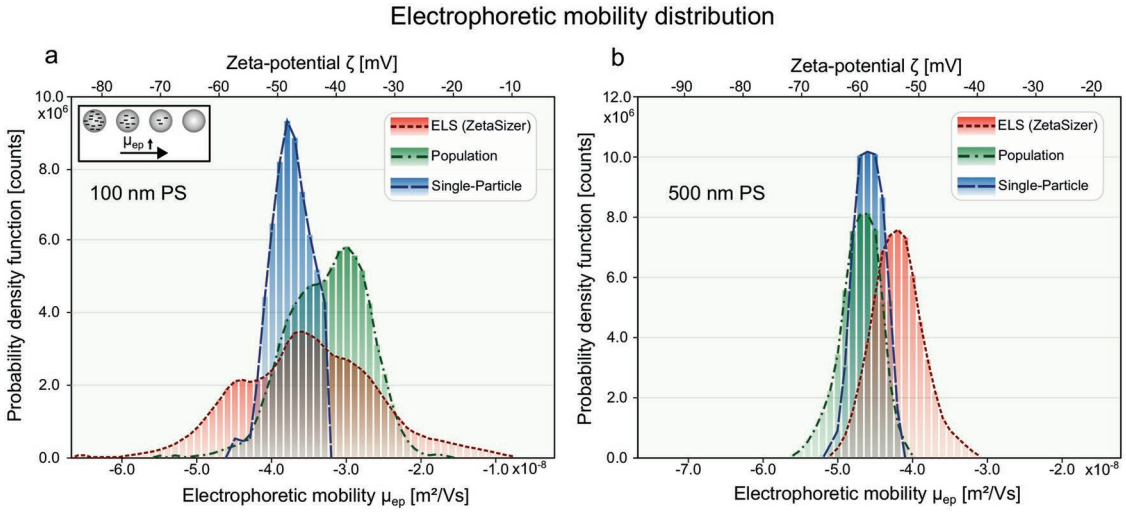

Figure 4. Electrophoretic mobility distributions for 100 and 500 nm particles (81 and 34 distinct particles respectively). a) For 100 nm particles, ELS data: $\overline{\mu}_{ep} \pm \sigma_{\overline{\mu}_{ep}} = (-3.5 \pm 0.9)\times10^{-8}$ m^2 V^{-1} s^{-1}; Population data: $\overline{\mu}_{ep} \pm \sigma_{\overline{\mu}_{ep}} = (-3.4 \pm 0.6)\times10^{-8}$ m^2 V^{-1} s^{-1}; Single-Particle data (selected): $\overline{\mu}_{ep} \pm \sigma_{\overline{\mu}_{ep}} = (-3.9 \pm 0.3)\times10^{-8}$ m^2 V^{-1} s^{-1}. b) For 500 nm particles, ELS data: $\overline{\mu}_{ep} \pm \sigma_{\overline{\mu}_{ep}} = (-4.0 \pm 0.3)\times10^{-8}$ m^2 V^{-1} s^{-1}; Population data: $\overline{\mu}_{ep} \pm \sigma_{\overline{\mu}_{ep}} = (-4.6 \pm 0.3)\times10^{-8}$ m^2 V^{-1} s^{-1}; Single-particle data: $\overline{\mu}_{ep} \pm \sigma_{\overline{\mu}_{ep}} = (-4.5 \pm 0.2)\times10^{-8}$ m^2 V^{-1} s^{-1}.

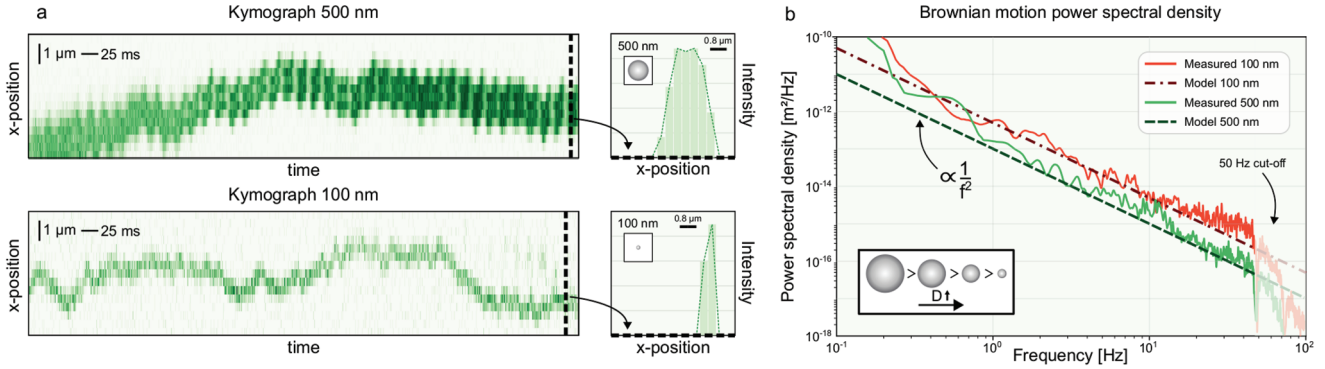

Figure 5. a) Comparison of kymographs of a 500 and a 100 nm particle measured along the *x*-axis perpendicular to the electric field. As expected, the 500 nm particle profile is distinctively broader than the 100 nm particle profile. b) Power spectral densities for ensembles of 100 and 500 nm particles (81 and 33 particles respectively) and the theoretical model.

simulation. This discrepancy in the field strength influences the average of the measurement distribution but not the spread. Nevertheless, by improving the microfluidic fabrication this issue can be circumvented. Additionally, reduction of the medium viscosity due to increasing temperatures can result in an overestimation of the mobility although as mentioned previously, precautions were taken to limit temperature build-up in the microchannel.

2.4. Particle Size from Brownian Motion

Where the electrophoretic mobility was measured from the individual particle motion parallel to the applied electric field, the particle size will be estimated from the free, Brownian motion along the axis perpendicular to the electric field. **Figure 5** shows the particle motion of individual particles (500 nm and 100 nm particles) along the *x*-axis (perpendicular to the *E*-field axis) and the power spectral densities $S(f)$ (PSD) of ensembles of 100 nm and 500 nm sized particles (81 and 33 particles respectively). From the kymographs in Figure 5a there is a clear qualitative distinction between the profiles of the 500 and 100 nm particles in an identical 16×16 pixel grid with 410 nm pixel pitch. Note that the 500 nm particle kymograph does show some periodic variation. This variation is caused by clipping of the particle profile during oscillation causing a periodic fluctuation of the photon count (see Supporting Information).

One way to estimate the particle size would be to use subpixel interpolation techniques and extensive analysis of the point spread function of calibration particles.[30,31] Here, we estimate the particle radius based on its Brownian motion, more specifically by analyzing the PSD of the measured Brownian motion. Since PS particles can be described as hard spheres (i.e., they maintain their shape unlike soft particles such as lipid NPs), the hydrodynamic radius is used as an estimation for the physical radius of the particles.[32] Hence, by estimating the diffusivity coefficient $D = \frac{k_B T}{6\pi\eta a}$, with a the hydrodynamic radius, the physical radius of a nanoparticle can be estimated. As described by Krapf et al.[33,34] the PSD of the Brownian motion of a single particle trace has a $1/f^2$ frequency dependence and scales linearly with the diffusivity coefficient D. Notice that for a singular particle trace of short duration an additional random amplitude factor A[33] scales the PSD, making it impossible to accurately estimate D. But, where the PSD of a single particle trace is described by $S(f) = A\frac{4D}{\omega^2}$ with ω the angular frequency, the PSD of a large ensemble of particles is described by $S(f) = \frac{4D}{\omega^2}$. Thus by combining multiple particle traces into a single long particle trace the PSD of the combined trace will approach $S(f) = \frac{4D}{\omega^2}$ as A approaches 1.

In Figure 5b the calculated PSDs are shown as the full red line (100 nm) and green line (500 nm) along with the PSD models (dash-dot for the 100 nm particles and dashed for the 500 nm particles) based on manufacturer values of respective particles (105 nm and 520 nm). The PSD of the 100 nm particles is based on a combined trace of 81 particles with a total duration of ≈30 s while the 500 nm particle trace is based on 33 particles also totaling to a 30 s position trace. The PSDs follow the aforementioned $1/f^2$ trend but drop off more steeply after the 50 Hz frequency due to a combined 50 Hz notch- and low-pass filtering done on the raw particle position trace to eliminate potential "leakage" of the oscillating movement from the perpendicular axis (though not eliminating the fluctuation of photon counts as previously mentioned). Therefore the final estimation of the diffusion coefficient was calculated for a frequency range between 3×10^{-4} and 49 Hz with a total of ≈600 meaningful values. The obtained diffusion coefficient D for the 100 nm particles is $D \pm \sigma_D = (6.5 \pm 2.4) \times 10^{-12}\ \mathrm{m^2\ s^{-1}}$ which results in a hydrodynamic radius of $a \pm \sigma_a = 43 \pm 15$ nm. Compared to the DLS measurements $a_{\mathrm{DLS}} \pm \sigma_{a_{\mathrm{DLS}}} = 56 \pm 12\,\mathrm{nm}$, the estimated value on the basis of 81 particles is lower, but lies within the standard deviation. The 500 nm particles have an estimated diffusion coefficient and hydrodynamic radius value of respectively: $D \pm \sigma_D = (1.9 \pm 0.7) \times 10^{-12}\ \mathrm{m^2\ s^{-1}}$ and $a \pm \sigma_a = 144 \pm 48$nm, compared to the DLS measurement result $a \pm \sigma_a = 280 \pm 110$nm our estimation is only half of the expected hydrodynamic radius. In the PSD curve, this offset compared to the model is also visible, but especially so between 5 and 10 Hz. This shows that size-analysis based on Brownian motion can distinguish particles based on size, but requires a larger number of particle traces.

3. Conclusion

We have presented a technique to measure the electrophoretic mobility of individual nanoparticles based on fast, sensitive laser-scanning microscopy and careful analysis of electroosmosis. By tracking the oscillation of individual particles in an electric field at high frame rates the velocity information is obtained containing contributions from both electrophoresis and electroosmosis. By using a theoretical model for electroosmosis and simulations of the electric field in a microfluidic channel, the electroosmotic effect can be subtracted, and the electrophoretic mobility can be calculated. The method is demonstrated for 100 and 500 nm fluorescent polystyrene beads in water with low conductivity. The dependency of the electroosmotic velocity on the position of the particle in the channel and the frequency and amplitude of the applied field agree well with the theoretical model. The nanoparticle size is characterized based on the analysis of the Brownian motion. As a result, the technique allows the characterization of two key parameters (charge and size) of fluorescent nanoparticles in a simple-to-manufacture microfluidic device. With future improvement of the SNR through optimization of the primary noise factors (by improving stray light shielding, confocal imaging on the SPCM, autofluorescence, and dichroic filtering) even smaller NPs can be characterized on the single particle level. Moreover, by adding the information contained within the amplitude and spectrum of the optical signal to the data processing a more extended multi-parameter analysis can be performed on a particle-to-particle basis. This allows the investigation of the correlations between nanoparticle properties and dynamics of nanoparticle interactions with their environment. Analyzing the size, charge, and optical properties at a high-throughput of single nanoparticles can provide unambiguous information on the quantity, distribution, and composition of nanoparticle ligands which are crucial to the developments of applications such as particle-based bioassays and nanomedicine formulation.

4. Experimental Section

Sample Preparation: The polystyrene particles were purchased from Spherotech inc. (500 nm) and Magsphere inc. (100 nm) and diluted in DI water to the desired concentration of one particle (or lower) per confocal volume based on the technical datasheet of the respective manufacturer.

DLS Measurements: The same samples prepared for the laser-scanning measurements were also measured with the Malvern Panalytical ZetaSizer Nano, resulting in the mobility and diffusivity values used in Section 2. In between sample measurements, the proprietary ZetaSizer capillary cell was cleaned using DI water and blow-dried using an air gun. Multiple measurements were performed per sample to ensure the stability of the results.

Microfluidic Device and Assembly: Microfluidic devices were constructed using two glass substrates (0.1 mm thick on the bottom and 1 mm thick at the top) separated by 100 µm spacer beads and assembled using UV curing glue (Norland Optical Adhesive 68). Before assembly, two holes were drilled in the top glass for inserting the electrodes and all glass substrates were cleaned using isopropyl alcohol and acetone and were rinsed with DI water. Then, both substrates were glued together with a rectangular pattern forming a microchannel with width of ≈10 mm and height of 100 µm. More details on the microfluidic cell geometry and assembly can be found in Supporting Information.

Scanning Laser Microscope and Microchannel Alignment: The optical setup (see full schematic in Supporting Information) consisted a custom-built inverted fluorescence microscope with 100× oil immersion objective (CFI Plan Fluor 100× Oil, Nikon), a high-speed CMOS camera (Zyla 4.2 sCMOS, Andor Instruments), and a green LED (M530L3, Thorlabs, 530 nm) for bright field Kohler illumination. This microscope was combined with a CW 532 nm collimated laser (L532-050-S, CrystalLaser) which was scanned using AODs (MT110-A1.5-VIS, AA Optoelectronic). The AOD-laser path can be split up in four parts. First, the laser beam power was set using an angle-adjustable half-wave plate combined with a polarizing beam splitter which divided the laser beam power over a direct laser illumination path and a scanning laser illumination path (see Supporting Information). Second, the laser beam was sent through a 3:1 beam reduction system to fit within the AOD aperture. Third, the laser beam with a reduced diameter was passed through the first AOD followed by a unity telescope and the second AOD. By passing the deflected laser beam through a unity telescope it was ensured that both AODs were in conjugate planes. Last, the deflected beam was filtered (masking the unwanted diffraction orders coming out of the AODs) and projected onto the microscope objective using a 1:4 beam expander with the second AOD center and microscope objective aperture as conjugate planes. Samples were clamped using an in-house built sample holder mounted on a 3D piezo nano-positioning stage (Tritor 102SG, Piezosystem Jena) for precise alignment. The 3D piezo stage was subsequently mounted on a vertical micro stage (MVS010/M, Thorlabs) and a 2D microstage for coarse position adjustment. A removable dichroic mirror allowed fast switching between bright field microscopy and epi-fluorescence (the scanning or direct laser). To increase sensitivity to the single photon level in epi-fluorescence mode, an SPCM was used (SPCM-AQRH-W5, Excelitas Technologies) equipped with a shutter for protection during bright field illumination.

In preparation for an experiment, the microfluidic channel was filled with the desired nanoparticle sample and visualized using bright field illumination. Once particles were observed, the bright field illumination was turned off and the direct laser was used to find the bottom of the microfluidic channel. By looking at the back reflection of the direct laser illumination on the CMOS the interface between the bottom glass substrate and the liquid can be found. At this glass-liquid interface, the 3D piezo stage was set to a zero value and the experimental height (z-position) of a particle can be determined with nanometer precision. At the desired z-position the direct laser was exchanged for the scanning laser illumination (by blocking and unblocking respective optical paths). After starting the FPGA program the SPCM shutter was opened and the power was adjusted based on a real-time photon count displayed on the controlling PC which recorded the FPGA data.

FPGA Control: An FPGA (PCIe-7842R, National Instruments) was programmed using the LabVIEW FPGA Module (National Instruments) on a host PC. The FPGA runs three parallel loops to apply a voltage over the microchannel (analog output), count photons (digital input), and drive the AOD voltages (analog outputs). Using separate direct memory access FIFO buffers, the input and output data was transferred from the FPGA to the host PC. To ensure synchronous reconstruction of the images from the saved data, a global register in the FPGA encoded the data in the FIFO buffers with a synchronization signal (see Supporting Information).

Particle Tracking and Centroid Location: The particle location was determined from the x-and y-profiles using a combination of centroid calculation and least square fitting with a Gaussian profile. The reconstructed frames were first filtered using a threshold background value and then the pixel values $I(m, n)$ were summed in the x- and y-direction to obtain the sum profiles

$$P_x = P(m) = \sum_{n=1}^{N} I(m,n); P_y = P(n) = \sum_{m=1}^{M} I(m,n) \tag{3}$$

From these profiles the pixel centroid (m_c, n_c) was calculated using $m_c = p\sum mP(m)/\sum P(m)$ for the x-profile and $n_c = p\sum nP(n)/\sum P(n)$ for the y-profile. Also, the standard deviation of the profiles was calculated

$$\sigma_m = \sqrt{\frac{1}{M}\sum P(m)(m-m_c)^2}; \sigma_n = \sqrt{\frac{1}{N}\sum P(n)(n-n_c)^2} \tag{4}$$

The calculated centroid (m_c, n_c) and spot size (σ_m, σ_n) qwre then used as the initial values for a least square fitting of a Gaussian profile to both *x*- and *y*-profiles. After fitting the Gaussian curve to each profile, the centers of the Gaussian patterns were taken as the final particle pixel location within a single frame. To then obtain the physical particle location, the pixel indices were multiplied by the respective pixel pitch. This procedure was repeated for each frame.

Supporting Information

Supporting Information is available from the Wiley Online Library or from the author.

Acknowledgements

The research of Lucas Oorlynck is funded by the Research Foundation-Flanders (FWO) through the Strategic Basic Research grant 1SD0721N.

Conflict of Interest

The authors declare no conflict of interest.

Data Availability Statement

The data that support the findings of this study are available from the corresponding author upon reasonable request.

Keywords

electroosmosis, electrophoresis, laser scanning microscopy, microfluidics, nanoparticles, particle tracking

Received: August 23, 2022
Revised: October 2, 2022
Published online: November 9, 2022

[1] K. Forier, K. Raemdonck, S. C. De Smedt, J. Demeester, T. Coenye, K. Braeckmans, *J. Controlled Release* **2014**, *190*, 607.
[2] J. B. Hall, M. A. Dobrovolskaia, A. K. Patri, S. E. McNeil, *Nanomedicine* **2007**, *2*, 6.
[3] S. C. De Smedt, J. Demeester, W. E. Hennink, *Pharm. Res.* **2000**, *17*, 2.
[4] C. K. Chen, P. K. Huang, W. C. Law, C. H. Chu, N. T. Chen, L. W. Lo, *Int. J. Nanomedicine* **2020**, *15*, 2131.
[5] K. Raemdonck, T. F. Martens, K. Braeckmans, J. Demeester, S. C. De Smedt, *Adv. Drug Delivery Rev.* **2013**, *65*, 1123.
[6] U. Sahin, K. Karikó, Ö. Türeci, *Nat. Rev.* **2014**, *13*, 759.
[7] B. Ning, Z. Huang, B. M. Youngquist, J. W. Scott, A. Niu, C. M. Bojanowski, K. J. Zwezdaryk, N. S. Saba, J. Fan, X. M. Yin, J. Cao, C. J. Lyon, C. Z. Li, C. J. Roy, T. Y. Hu, *Nat. Nanotechnol.* **2021**, *16*, 1039.
[8] B. S. Miller, L. Bezinge, H. D. Gilddon, D. Huang, G. Dold, E. R. Gray, J. Heaney, P. J. Dobson, E. Nastouli, J. J. L. Morton, R. A. McKendry, *Nature* **2020**, *587*, 588.
[9] P. J. Vikesland, *Nat. Nanotechnol.* **2018**, *13*, 651.
[10] T. Brans, F. Strubbe, C. Schreuer, K. Neyts, F. Beunis, *J. Appl. Phys.* **2015**, *117*, 214704.
[11] F. Ruggeri, F. Zosel, N. Mutter, M. Różycka, M. Wojtas, A. Ożyhar, B. Schuler, M. Krishnan, *Nat. Nanotechnol.* **2017**, *12*, 488.
[12] A. H. Squires, P. D. Dahlberg, H. Liu, N. C. M. Magdaong, R. E. Blankenship, W. E. Moerner, *Nat. Commun.* **2019**, *10*, 1172.
[13] A. Nel, T. Xia, L. Mädler, L. Ning, *Sci.* **2006**, *311*, 622.
[14] S. Zhang, H. Gao, G. Bao, *ACS Nano* **2015**, *9*, 9.
[15] R. Vogel, A. K. Pal, S. Jambhrunkar, P. Patel, S. S. Thakur, E. Reátegui, H. S. Parekh, P. Saá, A. Stassinopoulos, M. F. Broom, *Sci. Rep.* **2017**, *7*, 17479.
[16] F. Ruggeri, M. Krishnan, *Nano Lett.* **2018**, *18*, 3773.
[17] D. Sharma, R. Y. H. Lim, T. Pfohl, Y. Ekinci, *Microsyst. Nanoeng.* **2021**, *7*, 46.
[18] A. P. Fields, A. E. Cohen, *Chapter Seven - Anti-Brownian Traps for Studies on Single Molecules, Methods in Enzymology*, Vol. *475*, Academic Press, Cambridge, MA **2010**.
[19] A. H. Squires, A. A. Lavania, P. D. Dahlberg, W. Moerner, *Nano Lett.* **2019**, *19*, 4112.
[20] H. Wilson, Q. Wang, *Nat. Methods* **2021**, *18*, 816.
[21] G. Ma, Z. Wan, Y. Yang, P. Zhang, S. Wang, N. Tao, *Nat. Commun.* **2020**, *11*, 4768.
[22] G. S. Schlau-Cohen, S. Bockenhauer, Q. Wang, W. E. Moerner, *Chem. Sci.* **2014**, *5*, 2933.
[23] S. Sridharan, J. Zhu, G. Hu, X. Xuan, *J. Electrophor.* **2011**, *32*, 2274.
[24] S. H. Sadek, F. Pimenta, F. T. Pinho, M. A. Alves, *J. Electrophor.* **2017**, *38*, 1022.
[25] Since the aspect ratio of our microfluidic device is at least 1:10 we can approximate it as a one-dimensional channel independent of *x*- and *y*-coordinate.[26]
[26] C. Marcos Yang, T. N. Wong, K. T. Ooi, *Int. J. Eng. Sci.* **2004**, *42*, 1459.
[27] A. Page, D. Perry, P. Young, D. Mitchell, B. G. Frenguelli, P. R. Uwin, *Anal. Chem.* **2016**, *88*, 10854.
[28] L. Dorwling-Carter, M. Aramesh, H. Han, T. Zambelli, D. Momotenko, *Anal. Chem.* **2018**, *90*, 11453.
[29] J.-L. Fraikin, T. Teesula, C. M. McKenney, E. Ruoslahti, A. N. Cleland, *Nat. Nanotechnol.* **2011**, *6*, 308.
[30] H. Shen, L. J. Tauzin, R. Baiyasi, W. Wang, N. Moringo, B. Shuang, C. F. Landes, *Chem. Rev.* **2017**, *117*, 7331.
[31] C. Manzo, M. F. Gracia-Parajo, *Rep. Prog. Phys.* **2015**, *78*, 124601.
[32] B. Lin, J. Yu, S. A. Rice, *Phys. Rev. E* **2000**, *62*, 3909.
[33] D. Krapf, E. Marinari, R. Metzler, G. Oshanin, X. Xu, A. Squarcini, *New J. Phys.* **2018**, *20*, 023029.
[34] V. Sposini, R. Metzler, G. Oshanin, *New J. Phys.* **2019**, *21*, 073043.

